

# Finite-element simulation of firearm injury to the human cranium

A. Mota, W. S. Klug, M. Ortiz, A. Pandolfi

**Abstract** An advanced physics-based simulation of firearms injury to the human cranium is presented, modeling by finite elements the collision of a firearm projectile into a human parietal bone. The space-discretized equations of motion are explicitly integrated in time with Newmark's time-stepping algorithm. The impact of the projectile on the skull, as well as the collisions between flying fragments, are controlled through a nonsmooth contact algorithm. Cohesive theories of fracture, in conjunction with adaptive remeshing, control the nucleation and the propagation of fractures. The progressive opening of fracture surfaces is governed by a thermodynamically irreversible cohesive law embedded into cohesive-interface elements. Numerical results compare well with forensic data of actual firearm wounds to human crania.

**Keywords** Fracture, Fragmentation, Cohesive elements, Contact, Ballistic penetration, Firearm injury, Human cranium

## 1 Introduction

As simulation techniques become more accessible, both because of the availability of more powerful computers and the development of more advanced numerical methods, the ability to study otherwise inaccessible phenomena increases. Firearm injury to the human cranium is one such phenomenon. Since the late 1950s, firearm deaths have increased dramatically in the United States. In 1988, guns were responsible for 34 000 deaths, making them the eighth leading cause of death in this country. Fifty three

percent of the fatalities were suicides and forty percent were homicides; the remainder resulted from accidental shooting or were of undetermined cause. For each firearm-related death, there are seven people who sustain non fatal gunshot wounds. Gunshot wounds to the head have become the leading or second leading cause of head injury in many United States cities. They are also the most lethal of all firearm injuries. It is estimated that gunshot wounds to the head have a greater than 90% fatality rate for United States civilians, and at least two thirds of the victims die before reaching a hospital.

Much of what is known about how penetrating injuries damage the brain and how this damage is best treated, was learned from studying the many thousands of soldiers who received head injuries during World War II, Korea, and Vietnam. The predictors of neurological outcome after a gunshot wound to the head are presently quite primitive, and include the Glasgow Coma Scale score; age; presence of low blood pressure or inadequate oxygenation early after injury; and dilated non-reactive pupils. Not surprisingly, the bullet trajectory through the brain has major significance. Bullets that traverse the brain stem, multiple lobes of the brain, or the ventricular system (chambers where cerebrospinal fluid is located) are particularly lethal. Many initial survivors develop uncontrollable intracranial pressure and subsequently succumb. Virtually all cranial gunshot victims are aggressively resuscitated upon initial arrival at the hospital. If a patient's blood pressure and oxygenation can be maintained, an urgent CT scan of the brain is obtained. The decision to operate on a gunshot wound is based on three factors: the level of consciousness (GCS), the degree of brain stem neurological function, and the findings on the CT scan.

Most of the available physical evidence of damage from firearms comes from forensic medicine. Statistical analysis of data obtained from direct examination of wounds permits the establishment of correlations between the gunshot characteristics (speed, angle of impact, bullet caliber, and many others [20]), and the damage to the biological tissues. Effects of the angle of entrance are shown in images that follow. Figure 1 shows a skull damaged by a lateral impact, with entrance and exit wounds on the right and the left parietal bone respectively. Wounds produced by high-speed bullet impacting the skull under high angle are generally round or oval, with sharp, well defined edges [18–20], Fig. 2. When the bullet penetrates thicker bones, such as the mandible, the wound can assume an unusual shape, like that of a keyhole. Experimental gunshots on skull bone show that it is easily punctured, producing a

---

A. Mota (✉), W. S. Klug, M. Ortiz  
Graduate Aeronautical Laboratories,  
California Institute of Technology,  
Pasadena, CA 91125, USA

A. Pandolfi  
Dipartimento di Ingegneria Strutturale,  
Politecnico di Milano, 20133 Milano, Italy

Dedicated to the memory of Prof. Mike Crisfield, for his cheerfulness and cooperation as a colleague and friend over many years.

The authors would like to thank the W. M. Keck Foundation for their financial support for this research through the Keck Discovery Fund. Photographs in Figs. 1 and 2 provided by Valeri Craigle, Eccles Health Sciences Library, University of Utah, Copyright © 2000.

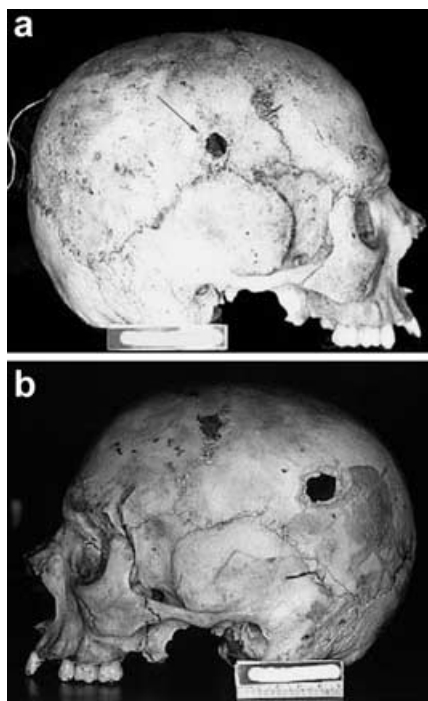


Fig. 1. Lateral impact on a skull. Entrance and exit wounds on right. a and left b parietal bones

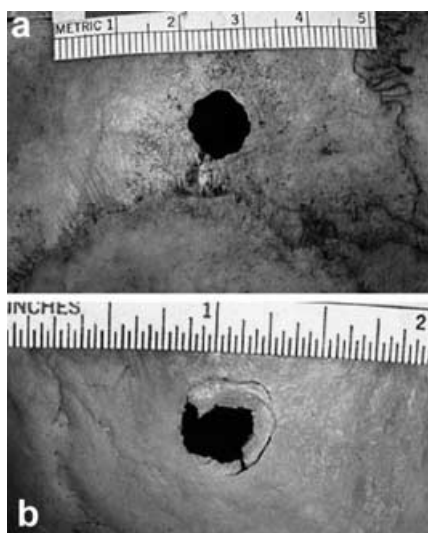


Fig. 2. Comparison between skull entrance wounds. In b, the hole shows a pronounced beveling

wound that is generally devoid of the extended radial cracks typical of blunt trauma [22]. However, in low-speed (less than 600 m/s) incidents, cranial cracks are sometimes observed radiating from localized bullet wounds (typically only entrance wounds) [3]. Entrance wounds are generally characterized by internal beveling [20], although external beveling has been reported [10, 16]. External beveling is common in exit wounds [20], for which internal beveling is seldom observed [4].

There is a paucity of observational evidence concerned with wounds resulting from projectile trajectories tangential to the cranium. Such wounds frequently show a

keyhole shape, sometimes with both internal and external beveling [4, 16, 18–20]. There is also limited insight into the correlation between wound dimensions and bullet characteristics. A correlation between bullet caliber and wound dimensions would be of practical interest when, for instance, the bullet is absent or lost. However, the establishment of such correlation is the object of some controversy [2, 21]. Other features, as the ratio between entrance wound area and exit wound area, are commonly well defined and accepted [19, 20].

A complete description of the injuries to the head tissues produced by a projectile would require an account of the mechanical and neurological damage on the involved organs. Unfortunately, the physical complexity of the human head is such that an exhaustive virtual description of its behavior is still unavailable, and unlikely to be obtainable in the short term.

Computer simulation, however, allows for the validation of forensic science findings and aids both the forensic and defense communities in enabling mechanics-based prediction of the fatality of the wounds. This in turn leads to improvements both in the understanding of the sequence of events in a firearm incident, for forensic science purposes, and the design of protective gear, such as helmets, for defense purposes. The main objective of this paper is to demonstrate the application of cohesive theories of fracture to direct finite element simulations of firearm injury to the human cranium. Specifically, we focus on the simulation of the ballistic penetration of the parietal bone by a pistol round. The simulation explicitly reproduces the impact, the nucleation of fracture, the extension of damage, and the scattering of comminuted bone fragments. The bullet-skull impact is described by means of the nonsmooth contact algorithm of Kane et al. [9]. The nucleation and propagation of fractures is modeled by the use of the self-adaptive fragmentation procedure of Pandolfi and Ortiz [14, 15], and by means of cohesive elements [12].

## 2 Methods

We explicitly simulate the impact between a bullet and the human parietal bone with a dynamic finite element analysis. The discretized equations of motion are integrated in time by Newmark's explicit time stepping algorithm. The two main issues of this simulation are the impact between projectile and cranium and the topological/geometrical changes related to the formation of fractures and fragments. We will briefly describe the algorithms used in the analysis. Exhaustive description of the procedures can be found in the original works ([9,13] for contact, [14,15] for fragmentation).

### 2.1 Constitutive modeling

The flat or "membrane" bones of the skull are composed in a sandwich-like fashion of an outer layer of compact bone (outer table), a middle layer of spongy bone (diploe) and an inner layer of compact bone (inner table). The ratio between the three layers thicknesses is variable, but precise data are not available. As estimate, in our application we

assume the ratio between the diploe and the inner/outer tables to be 1.

The constitutive behavior of bone is the result of the complementary properties of collagen (soft, ductile) and calcium phosphate (stiff, brittle) [24]. The mechanical properties of bone are related to the relative concentration of the two main components and to the orientation of the collagen fibers in the microstructure. As do almost all biological tissues, bone shows a strong rate dependency [23]. At low strain rates, the constitutive behavior is dominated by the organic component (collagen), and bone behaves as a relatively soft (low stiffness), ductile material (failure at relatively high strains). At higher strain rates, the mineral component (calcium phosphate) exerts greater influence, and bone exhibits higher stiffness and brittleness. At very high strain rates, the inorganic component fully characterizes the mechanical behavior: bone becomes stiff and brittle and failure occurs at relatively low strains. In consideration of the high strain rates of firearms impact, a stiff and brittle behavior is attributed to the bone tissue in the present numerical simulation. This behavior is well represented by a neo-hookean elastic constitutive model in combination with the model of brittle fracture of Sect. 2.3.

Disregarding its layered structure (which would require an extremely fine mesh), we model the parietal bone as homogeneous and isotropic. The elastic properties chosen for the “homogenized” bone are the average of the values for compact and spongy bone used by other authors in previous finite element analyses [25, 26]. The steel projectile, 9 mm caliber, is also modeled as elastic. The elastic properties for skull and projectile are collected in Table 1. The material properties for the cohesive constitutive law for the bone are shown in Table 2.

## 2.2

### Nonsmooth contact algorithm

In this work, we are concerned with nonsmooth contact situations – where corners and ridges are involved and the normal to the colliding surfaces is not univocally defined – and thus we invoke tools and algorithms typical of nonsmooth analysis [6].

In a continuum framework, contact situations arise when free trajectories of bodies in space are restricted by the presence of obstacles (i.e. fixed surfaces or other bodies). Obstacles in space can be expressed as algebraic inequalities of the coordinates identifying the configura-

tion of the bodies. We refer to these inequalities as impenetrability constraints. The set of trajectories of bodies that do not violate any impenetrability constraint is called admissible set  $C$ . The motion of a body with initial configuration  $B_0 \subset R^3$  is described by a deformation mapping  $\varphi : B_0 \times [0, T] \rightarrow R^3$  where  $[0, T]$  is the elapsed time interval [8, 11]. In presence of restrictions to the motion we define  $C$  as the set of all the one-to-one deformation mappings. Similar definitions apply to discretized systems and, in the following, we use the notation  $\varphi$  for a discretized deformation mapping and  $C$  for the set of admissible discretized configurations.

Under finite element discretization, impenetrability constraints are described by inequalities  $g_\alpha(\varphi) \geq 0$  of the nodal displacements [9, 13]. If  $N$  is the number of constraints, an alternative way to define the admissible set  $C$  is to include all the discretized deformation mappings satisfying the  $N$  non-negativity conditions:

$$\varphi \in C \iff g_\alpha(\varphi) \geq 0, \quad \alpha = 1, \dots, N \quad (1)$$

In the present context, the  $g_\alpha(\varphi)$  physically represent the overlapping volume between to inter-penetrating tetrahedral finite elements. Other possibilities exist, details about which can be found in [9, 13].

These contact constraints can be enforced by augmenting the mechanical energy of the system with an additional term expressing the contact energy. The contact energy contribution, called the indicator function  $I_C$ , is defined as:

$$I_C(\varphi) = \begin{cases} 0, & \text{if } \varphi \in C, \\ \infty, & \text{otherwise} \end{cases} \quad (2)$$

Thus the contact forces follow as the generalized gradient of the indicator function:

$$\mathbf{F}^{\text{con}}(\varphi) = \partial I_C(\varphi) \quad (3)$$

In this work, the contact constraints are implemented following a new class of nonsmooth contact algorithms for elastic bodies introduced by Kane et al. [9]. In summary, Kane’s algorithms re-write Newmark’s time stepping formula as a predictor/corrector contact algorithm where the predictor step provides an unconstrained configuration that identifies the violated constraints, and the corrector step returns the closest-point-projection of the predictor configuration onto the admissible set  $C$ . The closest-point-projection is obtained by solving a system of non-linear equations, or alternatively by performing a constrained minimization [9].

These algorithms have been proved to possess noticeable conservative properties for linear and angular momenta and, under non-restrictive conditions, mechanical energy as well [13]. Unfortunately, when numerous constraints are involved – as consequence of proliferation of fragments in brittle materials up to 100 000 constraints are violated at the same time – the procedure slows down considerably, requiring in some cases, prohibitive computational times. This difficulty can be overcome by adopting an approximate procedure based on a penalty approach. In the spirit of typical barrier methods, we approximate the indicator function as the sum of quadratic terms, one for each violated constraint:

**Table 1.** Elastic properties for steel and bone tissue

Material	$E$ (GPa)	$\nu$	$\rho$ (kg/m <sup>3</sup> )
Steel	201.0	0.30	7800.0
Bone	10.0	0.10	1700.0

**Table 2.** Cohesive properties for bone tissue

$G_c$ (N/m)	$\sigma_c$ (MPa)	$\delta_c$ ( $\mu\text{m}$ )	$\beta$
90.0	60.0	3.0	1.0

$$I_C(\boldsymbol{\varphi}) \approx \frac{1}{2} p \sum_{\alpha=1}^N g_\alpha^2(\boldsymbol{\varphi}) , \quad (4)$$

where  $p$  is a penalty parameter. The approximate contact forces are:

$$\mathbf{F}^{\text{con}}(\boldsymbol{\varphi}) \approx p \sum_{\alpha=1}^N g_\alpha(\boldsymbol{\varphi}) \nabla g_\alpha(\boldsymbol{\varphi}) \quad (5)$$

Following Kane et al. [9], we write the semi-discrete equations of motion in presence of contact as follows:

$$\mathbf{M}\ddot{\boldsymbol{\varphi}} + \mathbf{F}^{\text{int}}(\boldsymbol{\varphi}) + \mathbf{F}^{\text{con}}(\boldsymbol{\varphi}) = \mathbf{F}^{\text{ext}} \quad (6)$$

where  $\mathbf{M}$  is the lumped mass matrix, and  $\mathbf{F}^{\text{int}}(\boldsymbol{\varphi})$  and  $\mathbf{F}^{\text{ext}}$ , are the internal and external forces, respectively. We then discretize these equations in time via the explicit version of the Newmark time-stepping algorithm:

$$\begin{aligned} \mathbf{M}\mathbf{a}_{n+1} + \mathbf{F}^{\text{int}}(\boldsymbol{\varphi}_{n+1}) + \mathbf{F}^{\text{con}}(\boldsymbol{\varphi}_{n+1}) &= \mathbf{F}_{n+1}^{\text{ext}}, \\ \boldsymbol{\varphi}_{n+1} &= \boldsymbol{\varphi}_n + \Delta t \mathbf{v}_n + \frac{(\Delta t)^2}{2} \mathbf{a}_n, \\ \mathbf{v}_{n+1} &= \mathbf{v}_n + \frac{(\Delta t)^2}{2} (\mathbf{a}_n + \mathbf{a}_{n+1}) , \end{aligned} \quad (7)$$

in which  $\boldsymbol{\varphi}_n$ ,  $\mathbf{v}_n$ , and  $\mathbf{a}_n$  are approximations to  $\boldsymbol{\varphi}(t_n)$ ,  $\dot{\boldsymbol{\varphi}}(t_n)$ , and  $\ddot{\boldsymbol{\varphi}}(t_n)$ , respectively,  $\Delta t$  is the time step, and  $t_n$  the time at step  $n$ .

### 2.3

#### Fragmentation algorithm

Cohesive theories of fracture, pioneered by Dugdale and Barrenblatt [1, 7], describe the cracks as pairs of surfaces whose relative opening is resisted by cohesive forces in a manner which is independent of the bulk constitutive properties. Our approach to fracture and fragmentation is based on cohesive models embedded in surface-like cohesive elements [5, 12]. The power of a system with cohesive surfaces includes an additional term accounting for the work-conjugate cohesive quantities, i.e., the displacement jump  $\delta$  across the cohesive surface and the cohesive traction  $\mathbf{t}$ . Under finite element discretization, cohesive elements give an additional contribution to the internal forces  $\mathbf{F}^{\text{int}}(\boldsymbol{\varphi})$  in the semi-discrete equation of motion (6).

Following [5, 12], we define a cohesive energy density per unit of undeformed area  $\phi$  as:

$$\phi = \phi(\delta, \mathbf{q}; \mathbf{n})$$

where  $\mathbf{q}$  is a suitable collection of internal variables and  $\mathbf{n}$  is the normal to the deformed cohesive surface. The cohesive law follows from the thermodynamics laws:

$$\mathbf{t} = \frac{\partial \phi(\delta, \mathbf{q}; \mathbf{n})}{\partial \delta} .$$

Such a law can be derived in terms of two scalar parameters:  $\delta$ , the effective opening displacement; and  $t$ , the effective cohesive traction (see [12]). The irreversible cohesive law adopted in this analysis is drawn in Fig. 3, where  $\sigma_c$  is the cohesive traction limit and  $\delta_c$  is the critical opening displacement. The corresponding critical energy release rate is:

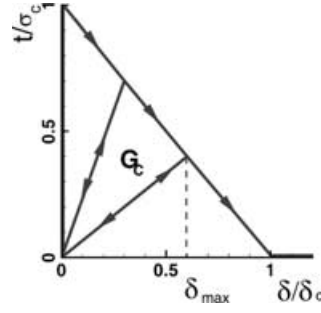


Fig. 3. Irreversible cohesive law, with linearly decreasing envelope

$$G_c = \frac{1}{2} \sigma_c \delta_c . \quad (8)$$

We explicitly simulate the formation of fracture surfaces with an automatic fragmentation procedure [14, 15]. We start with a fully coherent mesh, and assume that all the interfaces between adjacent finite elements are potential cohesive surfaces. The fragmentation procedure adaptively updates the discretized topology by inserting cohesive elements at high stress interfacial surfaces. The insertion criterion is based on the attainment of a critical value of the effective traction, i.e.,

$$t \geq \sigma_c \quad (9)$$

where  $\sigma_c$  is the cohesive strength of the material. Using the adaptive remeshing, cracks are allowed to nucleate, grow, branch and coalesce, eventually forming fragments.

### 3

#### Results

Figure 4 illustrates the initial mesh used in the numerical simulation. The model is discretized with 10-node quadratic tetrahedra, which are initially coherent. The number of nodes and elements for skull and projectile is reported in Table 3. During the analysis, the number of nodes and elements progressively increases, as consequence of the insertion of cohesive elements.

Although this work is not intended as a parametric study, two analyses were performed, each with a different projectile velocity. The initial projectile velocity was set to 600 m/s for the first analysis (henceforth referred as the slow simulation), and 1000 m/s for the second (fast simulation). The analyses were interrupted once the projectile had completely crossed the skull thickness; the impact was completed in 55  $\mu\text{s}$  for the slow bullet and in 33  $\mu\text{s}$  for the fast bullet. The penalty parameter  $p$  for the evaluation of the contact forces is set to  $10^{15}$ , a value which both prevents interpenetration and controls the magnitude of the contact forces. The stable time step is estimated by computing for each element the ratio of its inradius to its wave propagation speed, and then taking the minimum. The stable time step was computed every 10 steps due to the dependence of the wave speed on the deformation. Thus, the average time step used by the explicit integration was  $3 \times 10^{-4} \mu\text{s}$ . To reduce the computational time, contact was verified every 10 time steps, the proximity list was rebuilt every 100 time steps, and the fragmentation procedure was applied every 1000 time steps. Figures 5 and 6 show the

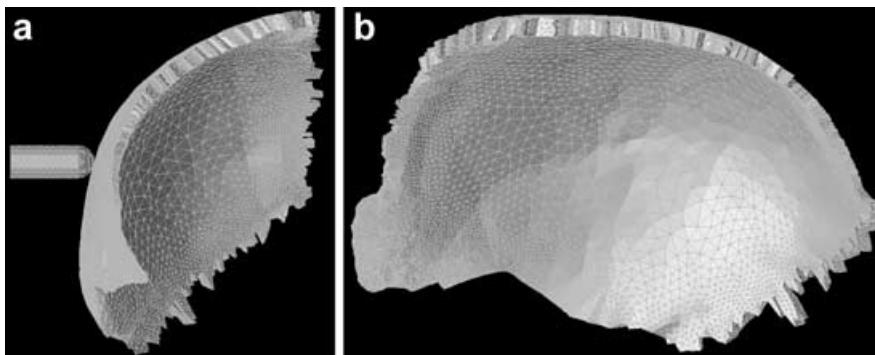


Fig. 4. Initial Finite Element Mesh: a Frontal view, b Lateral view

Table 3. Initial Nodes and Elements for Finite Element Mesh

	Nodes	Elements
Bullet	3197	2016
Bone	102981	51797
Total	106178	53813

results of the slow impact simulation. Figures 7 and 8 show the results for the fast impact simulation.

Both simulations show the presence of comminuted fragments, in keeping with forensic medicine observation of bullets impacting human bone. The presence of the bullet and of flying fragments prevents the evaluation of the actual wound size. To produce a cleaner sight of the final damage, the projectile and flying bone fragments have been removed from Figs. 9 and 10.

#### 4 Discussion

For sake of comparison, Fig. 11 shows a bullet crossing a human leg and penetrating the bone. Fragments are expelled both forward and backward with respect to the trajectory of the bullet. This phenomenon is also captured by the numerical simulation, see Figs. 5–8.

Figures 9–10 clearly show large circular wounds and no evidence of radial cracking, in agreement with the forensic observations. Although the correlation between bullet diameter and wound diameter does not appear to be well established, some data are available in the literature [21]. Table 4 collects data from forensic science for wound diameters. The diameter of the wound obtained in the numerical simulation is approximately 18 mm for the slow impact and 22 mm for the fast impact. Both the diameters are located towards the upper range of the experimental observation (see Table 4).

A few comments are appropriate in consideration of the small discrepancy between these results and forensic data. Firstly, the model does not include soft tissues (brain, meninges, outer skin). Reasonably, one might expect the interaction of such tissues to play a dissipative role, absorbing some of the energy from the impact, and thereby reducing the wound diameter. Secondly, the constitutive behavior assumed for bone tissue (non-linear elastic neo-hookean) does not account for rate dependency and dissipative effects consistent with the behavior of real bone. Thirdly, in the numerical simulation, the fragmentation

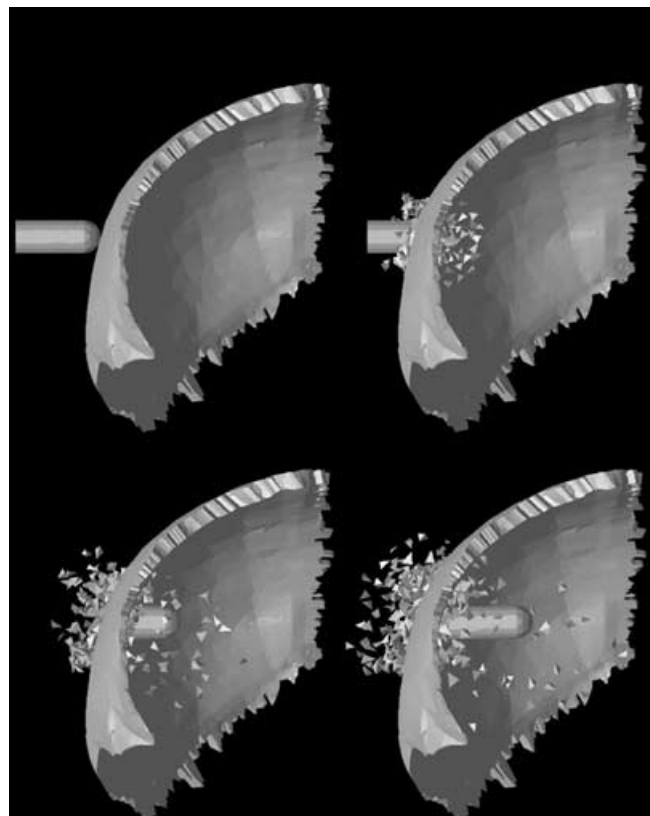


Fig. 5. Slow impact simulation: snapshots of the deformed configurations at 0, 18, 37 and 55  $\mu$ s after initial impact. Frontal view, external side

procedure was applied every 1000 time steps. In the time interval between fragmentation updates, if stresses in a region reach fracture-critical values, postponement of fracture until the next update time causes those stresses to continue building to unrealistic values. Then, once the next fracture check occurs, energy release in these regions of built-up stress can cause more damage to the bone than it would if the check had occurred before the stress build-up. The next fragmentation check detects several distant interfaces where the effective traction satisfies the insertion criterion (9). Finally, the use of the penalty-method enforcement of the contact constraints introduces a penalty parameter. A corresponding parametric study might show some variation in wound diameter. This and all other

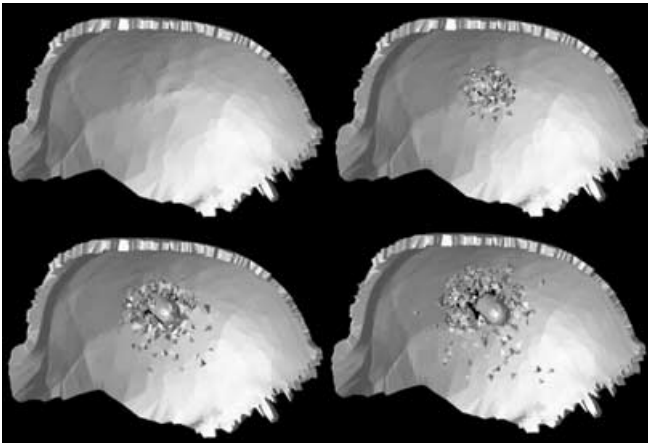


Fig. 6. Slow impact simulation: snapshots of the deformed configurations at 0, 18, 37 and 55  $\mu$ s after initial impact. Lateral view, brain side

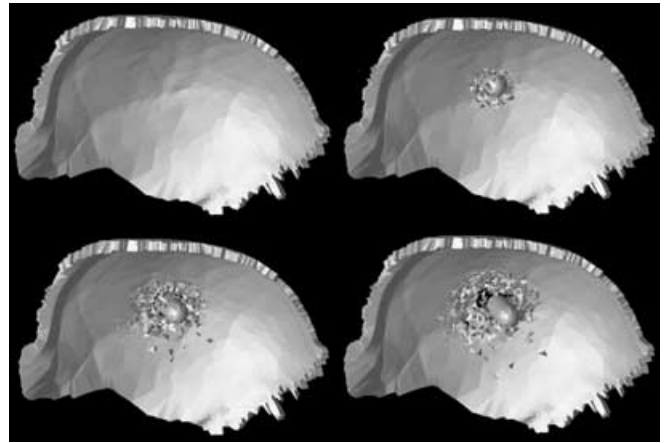


Fig. 8. Fast impact simulation: snapshots of the deformed configurations at 0, 11, 22 and 33  $\mu$ s after initial impact. Lateral view, brain side

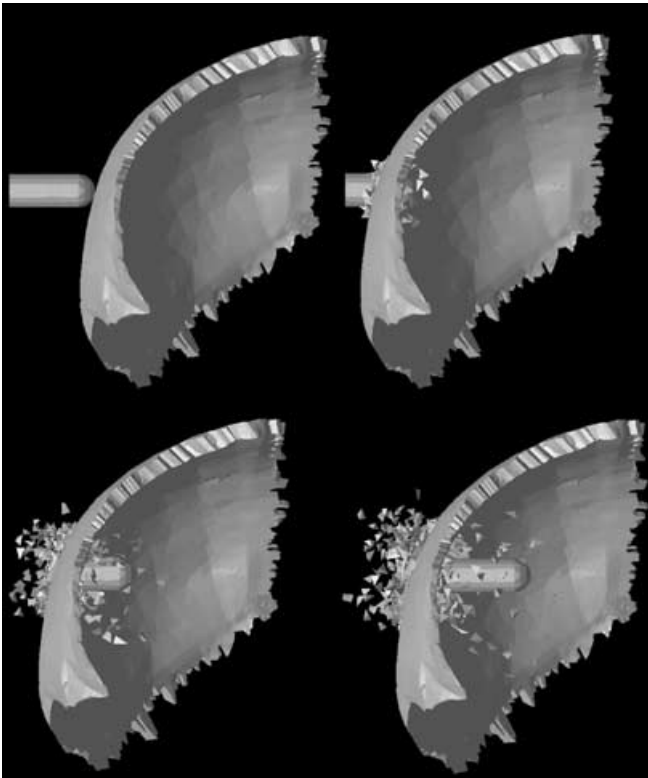


Fig. 7. Fast impact simulation: snapshots of the deformed configurations at 0, 11, 22 and 33  $\mu$ s after initial impact. Frontal view, external side

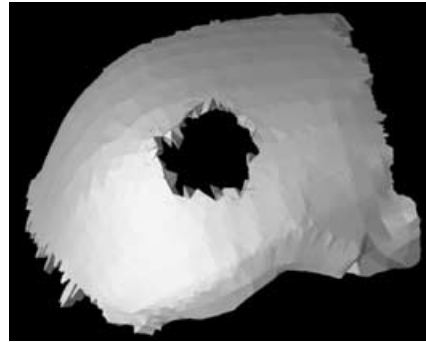


Fig. 9. Slow impact simulation: final configuration without bullet and flying fragments

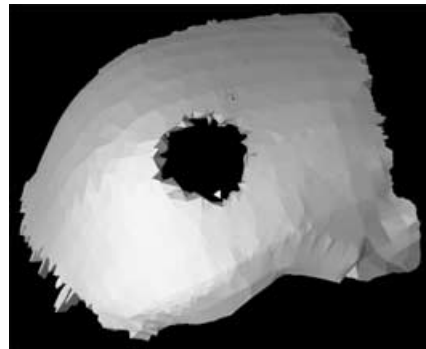


Fig. 10. Fast impact simulation: final configuration without bullet and flying fragments

mentioned simplifying approximations have been imposed by the available computational resources. The main drawback of the procedure is undoubtedly its sequential implementation, which precludes low-cost computations. A parallel version of these algorithms is currently under development.

Advanced head-injury simulation facilities such as described here provide a unique tool for investigating the mechanics of firearm injuries, including the effect of caliber, trajectory, and speed on the geometry and severity

of the injury; and for elucidating the effectiveness of protective gear such as helmets. Some of the possible benefits to industry, and the medical and defense communities, of such a facility include: the ability to derive a sound mechanistic – as opposed to merely statistical – understanding of traumatic head injury leading to improvements in operative management and post-traumatic care; and the ability to predict the lethality of firearm wounds to the head leading to improvements in helmet and other protective head-gear design and

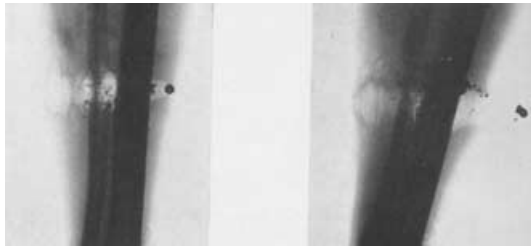


Fig. 11. Bullet penetrating a human leg [17]. Fragments expelled both forward and backward with respect to bullet trajectory

Table 4. Entrance wound diameters [21].  $N$  is the number of observed wounds;  $\mu$  is the mean diameter;  $\sigma$  is the standard deviation

Caliber (in, mm)	$N$	$\mu$ (mm)	$\sigma$ (mm)	min (mm)	max (mm)
Minimum					
0.22, 5.59	37	6.76	1.27	5.6	11.5
0.25, 6.35	5	6.72	0.66	6.0	7.5
0.32, 8.13	6	8.67	1.52	6.6	10.9
0.38, 9.65	25	11.00	2.33	8.7	17.4
Maximum					
0.22, 5.59	37	8.49	2.23	5.9	16.7
0.25, 6.35	4	8.58	1.64	6.3	10.0
0.32, 8.13	6	10.77	2.37	7.0	15.0
0.38, 9.65	23	12.88	3.42	9.4	22.0
Average					
0.22, 5.59	16	7.62	1.68	5.6	10.9
0.25, 6.35	8	7.11	0.94	5.4	9.1
0.38, 9.65	11	11.68	1.75	8.1	18.2

increased survivability during live-fire events. Finally, advanced simulation may assist defendants and insurance companies during personal injury litigation by providing a basis for expert witness, including injury and accident reconstruction and failure analysis.

## References

1. Barrenblatt GI (1962) The mathematical theory of equilibrium of cracks in brittle fracture. *Adv. Appl. Mech.* 7: 55–129
2. Berryman HE, Smith OC, Symes SA (1995) Diameter of cranial gunshot wounds as a function of bullet caliber. *J. Forensic Sci.* 40(5): 751–754
3. Betz P, Stiefel D, Eisenmenger W (1996) Cranial fractures and direction of fire in low velocity gunshots. *Int. J. Legal Med.* 109(2): 58–61
4. Bhoopat T (1995) A case of internal beveling with an exit gunshot wound to the skull. *Forensic Sci. Int.* 71(2): 97–101
5. Camacho GT, Ortiz M (1996) Computational modelling of impact damage in brittle materials. *Int. J. Sol. Struct.* 33: 2899–2938
6. Clarke FH (1983) *Optimization and Nonsmooth Analysis*. John Wiley & Sons, New York
7. Dugdale DS (1960) Yielding of steel sheets containing slits. *J. Mech. Phys. Soli.* 8: 100–104
8. Gurtin ME (1981) *An Introduction to Continuum Mechanics*. Academic Press, San Diego, California
9. Kane C, Repetto ER, Ortiz M, Marsden JE (1999) Finite element analysis of nonsmooth contact. *Comput. Meth. Appl. Mech. Eng.* 180(1–2): 1–26
10. Lantz PE (1994) An atypical, indeterminate-range, cranial gunshot wound of entrance resembling and exit wound. *Am. J. Forensic Med. Pathol.* 15(1): 5–9
11. Marsden JE, Hughes TJR (1983) *Mathematical Foundations of Elasticity*. Prentice-Hall, Englewood Cliffs, New Jersey
12. Ortiz M, Pandolfi A (1999) Finite-deformation irreversible cohesive elements for three-dimensional crack-propagation analysis. *Int. J. Numer. Meth. Eng.* 44(9): 1267–1282
13. Pandolfi A, Cane K, Marsden JE, Ortiz M (2002) Time-discretized variational formulation of non-smooth frictional contact. *Int. J. Numer. Meth. Eng.* 53: 1801–1829
14. Pandolfi A, Ortiz M (1998) Solid modeling aspects of three-dimensional fragmentation. *Eng. Comput.* 14(4): 287–308
15. Pandolfi A, Ortiz M (2002) An efficient adaptive procedure for three-dimensional fragmentation simulations. *Eng. Comput.* 18: 148–159
16. Peterson BL (1991) External beveling of cranial gunshot entrance wounds. *J. Forensic Sci.* 36(5): 1592–1595
17. Piédelièvre, Michon R (1954) Recent developments in legal medicine due to the use of high-speed photography, radiography and cinematography. In: *Proceedings of the Second International Congress of High-Speed Photography, Paris* 390–392
18. Quatrehomme G, İşcan MY (1998) Analysis of beveling in gunshot entrance wounds. *Forensic Sci. Int.* 93(1): 45–60
19. Quatrehomme G, İşcan MY (1998) Gunshot wounds to the skull: comparison of entries and exits. *Forensic Sci. Int.* 94 (1–2): 141–146
20. Quatrehomme G, İşcan MY (1999) Characteristics of gunshot wounds in the skull. *J. Forensic Sci.* 44(3): 568–576
21. Ross AH (1996) Caliber estimation from cranial entrance defect measurements. *J. Forensic Sci.* 41(4): 629–633
22. Schyma C, Bittner M, Placidi P (1997) The men frangible – study of a new bullet in gelatin. *Am. J. Forensic Med. Pathol.* 18(4): 325–330
23. Silver FH (1999) *Biomaterials Science and Biocompatibility*. Springer-Verlag, New York
24. Suchanek W, Yoshimura M (1998) Processing and properties of hydroxyapatite-based biomaterials for use as hard tissue replacement implants. *J. Mater. Res.* 13(1): 94–117
25. Willinger R, Kang HS, Diaw BM (1999) Développement et validation d'un modèle mécanique de la tête humaine. *Bio-mécanique* 327(1): 125–131
26. Willinger R, Kang HS, Diaw BM (1999) Modélisation de la boîte crânienne et du cerveau sous un impact. *Revue Française de Mécanique*, 1999(3): 179–185